EARTHQUAKE ENGINEERING AND STRUCTURAL DYNAMICS
Earthquake Engng Struct. Dyn. 2000; **29**: 419–439

Scattering of elastic waves by a 3D anisotropic basin

T. Zheng and M. Dravinski*

University of Southern California, Los Angeles CA 90089-1453, U.S.A.

SUMMARY

Scattering of elastic waves by a three-dimensional transversely isotropic basin of arbitrary shape embedded in a half-space is considered using an indirect boundary integral equation approach. The unknown scattered waves are expressed in terms of point sources distributed on the so-called auxiliary surfaces. The sources are expressed in terms of the full-space Green's functions with their intensities determined from the requirement that the boundary and the continuity conditions are to be satisfied in the least-squares sense. Steady-state results were obtained for incident plane pseudo-P-, SH-, SV-, and Rayleigh waves.

Using the Radon transform the Green's functions are obtained in the form of finite integrals over a unit sphere or a unit circle which can be numerically evaluated very efficiently.

Detailed analysis of the method includes the discussion on the shape of the auxiliary surfaces and the distribution of the collocation points and sources. The convergence criteria is defined in terms of transparency tests, isotropic limit test, and minimization of a certain norm. The isotropic limit tests show excellent agreement with the isotropic results available in literature.

For anisotropic materials the numerical results are given for a semispherical basin. The results show that presence of an anisotropic basin may result in significant amplification of surface motion atop the basin. While the amplitude of peak surface motion may be similar to the corresponding isotropic results, the difference in the displacement patterns may be quite different between the two. Therefore, this study clearly demonstrates that material anisotropy may be very important for accurate assessment of surface ground motion amplification atop basins. Copyright © 2000 John Wiley & Sons, Ltd.

KEY WORDS: three-dimensional anisotropic basin; site response

1. INTRODUCTION

Scattering of waves by isotropic subsurface inclusion has been the subject of many studies in geophysics and non-destructive material testing (e.g., [1–4]). These studies provide reasonable understanding of the wave scattering for isotropic models. Corresponding problem involving anisotropic media is characterized by far greater complexities and consequently there are much fewer studies available on the topic. One of the earlier investigations on the role of anisotropy in surface layers of the Earth is due to Stonley [5]. He demonstrated that presence of transversely

* Correspondence to: M. Dravinski, Department of Mechanical Engineering, University of Southern California, Los Angeles, CA 90089-1453, U.S.A.

Received 4 May 1999
Accepted 14 September 1999

isotropic materials may result in significant differences in wave propagation compared to motion in isotropic materials. However, modelling the scattering of waves in anisotropic media leads to additional difficulties associated with accurate and efficient evaluation of the corresponding Green's functions. The standard Fourier transform technique requires integration over an infinite four-dimensional space which is hard to accomplish numerically [6, 7]. Consequently, these studies have been confined mainly to two-dimensional problems [8–10].

Recently, several researchers approached the solution of the problem of the Green's functions in an anisotropic medium by using the Radon transform [7, 11]. The Radon transform has been studied extensively in computational tomography [12]. The key feature of this transform is that it reduces a three-dimensional wave equation to a one-dimensional differential equation. Furthermore, the inverse Radon transform can be expressed in terms of integrals over the surface of a unit sphere which are easy to evaluate numerically. These advances in the Green's functions analysis facilitated the research on scattering of waves in anisotropic media which is considered in this paper.

2. STATEMENT OF PROBLEM

Geometry of the problem is depicted by Figure 1. The model consists of a half-space $(D_1 : |x_1, x_2| \leqslant \infty; 0 \leqslant x_3 \leqslant \infty)$ with a three-dimensional basin of arbitrary shape D_2. The domains of the half-space and the basin are denoted by D_1 and D_2, respectively. The interface C between the basin and the half-space is assumed to be sufficiently smooth. Materials are assumed to be linearly elastic, homogeneous and transversely isotropic exhibiting symmetry with respect to arbitrary rotations about the x_3-axis [13].

The steady-state equations of motion can be written as

$$\sigma_{ij,j} + \rho\omega^2 u_i = 0;\ i, j = 1, 2, 3;\ (\ )_{,j} \equiv \frac{\partial}{\partial x_j} \tag{1}$$

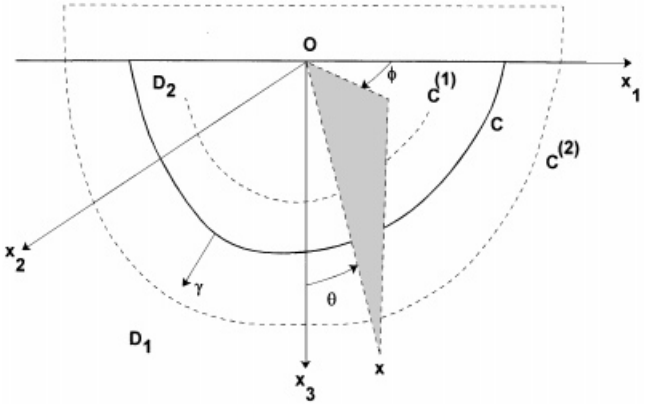

Figure 1. Geometry of the problem.

and the linearized stress–strain relation is given by

$$\sigma_{ij} = c_{ijpq} e_{pq};\ i, j, p, q = 1, 2, 3 \tag{2}$$

where e_{pq}, σ_{ij}, ρ, ω, and c_{ijpq} are the strain tensor, the stress tensor, the mass density, the circular frequency, and the tensor of elastic constants, respectively. Throughout the paper summation over repeated indices is assumed. Underlined indices indicate that the summation convention over repeated indices is being suppressed. The strain tensor components are defined by

$$e_{pq} = \tfrac{1}{2}(u_{p,q} + u_{q,p}) \tag{3}$$

where u_p denotes the displacement vector. The symmetry of the stress and strain tensors, and the existence of the positive strain energy density function imply the symmetry and positive definiteness of c_{ijpq}

$$\begin{gathered} c_{ijpq} = c_{jipq} = c_{ijqp} = c_{pqij} \\ c_{ijpq} e_{ij} e_{pq} > 0 \end{gathered} \tag{4}$$

for any non-zero real-valued tensor e_{ij}. Thus, in general, out of 81 components of c_{ijpq} only 21 are independent. In particular, the constitutive equations for transversely isotropic material involve five material constants and they can be written as [13]

$$\begin{bmatrix} \sigma_{11} \\ \sigma_{22} \\ \sigma_{33} \\ \sigma_{23} \\ \sigma_{13} \\ \sigma_{12} \end{bmatrix} = \begin{bmatrix} C_{11} & C_{12} & C_{13} & 0 & 0 & 0 \\ C_{12} & C_{11} & C_{13} & 0 & 0 & 0 \\ C_{13} & C_{13} & C_{33} & 0 & 0 & 0 \\ 0 & 0 & 0 & C_{44} & 0 & 0 \\ 0 & 0 & 0 & 0 & C_{44} & 0 \\ 0 & 0 & 0 & 0 & 0 & C_{66} \end{bmatrix} \begin{bmatrix} e_{11} \\ e_{22} \\ e_{33} \\ 2e_{23} \\ 2e_{13} \\ 2e_{12} \end{bmatrix} \tag{5}$$

where $C_{66} = (C_{11} - C_{12})/2$. In order to relate $c_{ijpq}(i, j, p, q = 1, 2, 3)$ to $C_{kl}(k, l = 1, 2, \ldots, 6)$ the following subscript contracting convention has been used: $1 \to 11$, $2 \to 22$, $3 \to 33$, $4 \to 23$, $5 \to 13$, and $6 \to 12$. Thus, for example, $c_{1122} \to C_{12}$ and so on.

The stress-free boundary conditions are given by

$$\sigma_{33}^{(J)} = \sigma_{32}^{(J)} = \sigma_{31}^{(J)} = 0; \quad x_3 = 0, \mathbf{x} \in D_J;\ J = 1, 2 \tag{6}$$

where the superscript (J) denotes the domain D_J. Perfect bonding along the interface C between the half-space and the basin can be stated as

$$u_i^{(1)} = u_i^{(2)}, \quad i = 1, 2, 3; \mathbf{x} \in C \tag{7}$$

$$t_i^{(1)} = t_i^{(2)}, \quad i = 1, 2, 3; \mathbf{x} \in C \tag{8}$$

where $t_i = \sigma_{ij}\gamma_j$ are components of the traction vector and γ denotes unit normal vector on C (Figure 1).

The incident field is assumed to be a plane harmonic wave. As the incident wave strikes the basin it generates scattered waves. These interact with the free-field resulting in amplification (constructive interference) or reduction (destructive interference) of motion. The objective of the paper is to determine the unknown scattered waves and subsequently the total displacement and stress field throughout the medium.

3. SOLUTION OF PROBLEM

As the incident wave strikes the interface C, it is partially transmitted into the basin and partially reflected back into the half-space. Consequently, the waves in the half-space consist of the free field and the scattered wave field, while the motion inside the basin comprises of the scattered waves only. Therefore, the displacement components in the half-space and the basin can be expressed as

$$\begin{aligned} u_i^{(1)} &= u_i^{\mathrm{ff}} + u_i^{(1)\mathrm{s}}; \quad \mathbf{x} \in D_1 \\ u_i^{(2)} &= u_i^{(2)\mathrm{s}}; \quad \mathbf{x} \in D_2; \quad i = 1, 2, 3 \end{aligned} \tag{9}$$

where the superscripts s and ff denote the scattered and free fields, respectively. For different incident waves the free field results are given in References [10, 13].

For the indirect integral equation approach considered in this paper, the scattered wave field is assumed to be expressed in terms of single layer potentials [14, 15]

$$u_p^{(J)}(\mathbf{x}, \omega) = \int_{C^{(J)}} q_k^{(J)}(\mathbf{y}) g_{pk}^{(J)}(\mathbf{x}, \mathbf{y}, \omega)\, \mathrm{d}\mathbf{y}, \quad \mathbf{x} \in \mathbf{D}_J, \quad J = 1,2, \quad p, k = 1, 2, 3 \tag{10}$$

where $q_k^{(J)}$ are the unknown density functions, $C^{(J)}$ are auxiliary surfaces defined [16] by Figure 1, and summation convention do not apply to repeated superscripts. $g_{pk}^{(J)}(\mathbf{x}, \mathbf{y}, \omega)$ are components of full-space Green's function tensor which satisfy the following equations of motion:

$$\{\Gamma_{ip}^{(J)} + \rho^{(J)}\omega^2\delta_{ip}\}\, g_{pk}^{(J)}(\mathbf{x}, \mathbf{y}, \omega) = -\delta_{ik}\delta(\mathbf{x} - \mathbf{y}) \tag{11}$$

where

$$\Gamma_{ip}^{(J)} = c_{ijpq}^{(J)} \frac{\partial}{\partial x_j} \frac{\partial}{\partial x_q}, \quad i, j, k, p, q = 1, 2, 3 \tag{12}$$

and the factor $\mathrm{e}^{-\mathrm{i}\omega t}$ is understood. Corresponding Green's function stresses are given by

$$h_{ijk}^{(J)}(\mathbf{x}, \mathbf{y}, \omega) = c_{ijpq}^{(J)} g_{pk,q}^{(J)}(\mathbf{x}, \mathbf{y}, \omega) \tag{13}$$

The explicit expressions of the Green's functions, can be found in the paper by Wang and Achenbach [11].

If the unknown density functions are assumed in the form of discrete point sources, i.e.

$$\begin{aligned} q_1^{(1)}(\mathbf{x}_0) &= a_m \delta(\mathbf{x}_0 - \mathbf{x}_m) \\ q_2^{(1)}(\mathbf{x}_0) &= b_m \delta(\mathbf{x}_0 - \mathbf{x}_m) \\ q_3^{(1)}(\mathbf{x}_0) &= c_m \delta(\mathbf{x}_0 - \mathbf{x}_m), \quad \mathbf{x}_m \in C^{(1)}, \quad m = 1, \ldots, M \\ q_1^{(2)}(\mathbf{x}_0) &= d_m \delta(\mathbf{x}_0 - \mathbf{x}_\ell) \\ q_2^{(2)}(\mathbf{x}_0) &= e_m \delta(\mathbf{x}_0 - \mathbf{x}_\ell) \\ q_3^{(2)}(\mathbf{x}_0) &= f_m \delta(\mathbf{x}_0 - \mathbf{x}_\ell), \quad \mathbf{x}_\ell \in C^{(2)}, \quad \ell = 1, \ldots, L \end{aligned} \tag{14}$$

then the scattered wave field becomes

$$u_p^{(1)} = a_m g_{p1}^{(1)}(\mathbf{x}, \mathbf{x}_m, \omega) + b_m g_{p2}^{(1)}(\mathbf{x}, \mathbf{x}_m, \omega) + c_m g_{p3}^{(1)}(\mathbf{x}, \mathbf{x}_m, \omega)$$
$$u_p^{(2)} = d_\ell g_{p1}^{(2)}(\mathbf{x}, \mathbf{x}_\ell, \omega) + e_\ell g_{p2}^{(2)}(\mathbf{x}, \mathbf{x}_\ell, \omega) + f_\ell g_{p3}^{(2)}(\mathbf{x}, \mathbf{x}_\ell, \omega) \tag{15}$$
$$p = 1, 2, 3, \quad m = 1, \ldots, M, \quad \ell = 1, \ldots, L$$

where the coefficients a_m to f_ℓ are still to be determined and M and L denote the number of sources along the auxiliary surfaces $C^{(1)}$ and $C^{(2)}$, respectively. These coefficients will be evaluated through the stress free boundary conditions (6) and the continuity conditions (7) and (8). Since the free field already satisfies the stress free boundary conditions at the surface of the half-space, Equation (6) for the domain D_1 involves only the scattered wave field, i.e.

$$\sigma_{3k}^{(1)s} = 0, \quad x_3 = 0, \quad k = 1, 2, 3, \quad \mathbf{x} \in D_1 \tag{16}$$

By imposing these conditions at P locations at the surface of the half-space $\{\mathbf{x}_p \in D_1 | x_3 = 0; p = 1, \ldots, P\}$ Equation (16) can be written in the following form:

$$\mathbf{H}^{(1)} \begin{bmatrix} \mathbf{a} \\ \mathbf{b} \\ \mathbf{c} \end{bmatrix} = \mathbf{0} \tag{17}$$

where the matrix $\mathbf{H}^{(1)}$ is given in the appendix and $\mathbf{a} = [a_m]$, $\mathbf{b} = [b_m]$, and $\mathbf{c} = [c_m]$ denote the vectors of the unknown coefficients.

Similarly, the stress free boundary conditions for the basin imposed at $\mathbf{x}_q \in \{\mathbf{D}_2 | x_3 = 0; q = 1, \ldots, Q\}$ become

$$\mathbf{H}^{(2)} \begin{bmatrix} \mathbf{d} \\ \mathbf{e} \\ \mathbf{f} \end{bmatrix} = \mathbf{0} \tag{18}$$

where the matrix $\mathbf{H}^{(2)}$ is known (see the appendix) and $\mathbf{d} = [d_\ell]$, $\mathbf{e} = [e_\ell]$, $\mathbf{f} = [f_\ell]$ denote the unknown coefficient vectors. This completes the formulation of the stress free boundary conditions.

The continuity conditions for displacement field along the interface C imposed at $\mathbf{x}_n \in C$; $n = 1, \ldots, N$, follow to be

$$[\mathbf{G}^{(1)} \quad -\mathbf{G}^{(2)}]\mathbf{g} = -\mathbf{u}^{(1)\mathrm{ff}} \tag{19}$$

where the matrices $\mathbf{G}^{(1)}$, $\mathbf{G}^{(2)}$, and vector $\mathbf{u}^{(1)\mathrm{ff}}$ are known (see the appendix) while vector $\mathbf{g}$ contains all the unknown coefficient vectors

$$\mathbf{g}^{\mathrm{T}} = [\mathbf{a}, \mathbf{b}, \mathbf{c}, \mathbf{d}, \mathbf{e}, \mathbf{f}]^{\mathrm{T}}$$

On the other hand, the continuity of the tractions along the interface C imposed at $\mathbf{x}_n \in C$; $n = 1, \ldots, N$, can be written as

$$[\mathbf{T}^{(1)} \quad -\mathbf{T}^{(2)}]\mathbf{g} = -\mathbf{t}^{(1)\mathrm{ff}} \tag{20}$$

where matrices $\mathbf{T}^{(1)}$ and $\mathbf{T}^{(2)}$ and vector $\mathbf{t}^{(1)\mathrm{ff}}$ are known (see the appendix).

Therefore, the stress free boundary conditions along the half-space surface and the continuity conditions along the interface C can be combined into the following equation:

$$\mathbf{Ag} = \mathbf{w} \tag{21}$$

Here

$$\mathbf{A} = \begin{bmatrix} \mathbf{H}^{(1)} & \mathbf{0} \\ \mathbf{G}^{(1)} & -\mathbf{G}^{(2)} \\ \mathbf{T}^{(1)} & -\mathbf{T}^{(2)} \\ \mathbf{0} & \mathbf{H}^{(2)} \end{bmatrix} \tag{22}$$

$$\mathbf{w} = \begin{bmatrix} \mathbf{0} \\ -\mathbf{u}^{(1)\mathrm{ff}} \\ -\mathbf{t}^{(1)\mathrm{ff}} \\ \mathbf{0} \end{bmatrix} \tag{23}$$

Equation (21) represents $3(P + Q + 2N)$ equations in $3(M + L)$ unknowns, which is solved in the least-squares sense by using QR-decomposition.

4. NUMERICAL PROCEDURE

This section deals with specific numerical issues which arise in the indirect boundary integral equation approach used in the paper. The section consists of four parts. The first part addresses the numerical evaluation of the Green's functions for anisotropic media. The second part deals with the auxiliary surfaces while the third part describes the location of collocation points and sources. The convergence criteria is discussed in part four.

4.1 Green's functions evaluation

The key component in evaluation of numerical results lies in developing an efficient algorithm for calculation of the Green's functions. This problem is briefly addressed next.

In general, the standard Fourier transform approach in evaluation of the Green's functions requires integration over an infinite four-dimensional space which is difficult to accomplish numerically [6, 7]. Consequently, this method has been used mainly to two-dimensional problems [9, 10]. Recently, several researchers derived the Green's functions in anisotropic media by using the Radon transform [7, 11]. The key feature of the Radon transform approach is that the Green's functions can be written in terms of integrals over a unit circle and a unit sphere. This technique has been used for evaluating the Green's function in the present paper. A brief outline of the procedure is presented as follows.

By using a three-dimensional Radon transform, defined by the following pair of equations [12]:

$$\Re\{f(\mathbf{x})\} = \hat{f}(s, \mathbf{n}) = \int f(\mathbf{x})\delta(s - \mathbf{n}\cdot\mathbf{x})\,\mathrm{d}\mathbf{x} \tag{24}$$

$$f(\mathbf{x}) = -\frac{1}{8\pi^2}\int_{|\mathbf{n}|=1}\left[\frac{\partial^2 \hat{f}(\mathbf{s}, \mathbf{n})}{\partial s^2}\right]_{s=\mathbf{n}\cdot\mathbf{x}} \mathrm{d}S(\mathbf{n}) \tag{25}$$

Wang and Achenbach [11] showed that the displacement Green's functions can be written in the following form:

$$g_{pk}(\mathbf{x}, \omega) = g^{\mathrm{S}}_{pk}(\mathbf{x}) + g^{\mathrm{R}}_{pk}(\mathbf{x}, \omega); \quad p, k = 1, 2, 3 \tag{26}$$

where the superscripts S and R denote the singular (static) and regular (dynamic) parts, respectively. The regular and singular parts are given by

$$g^{\mathrm{S}}_{pk}(\mathbf{x}) = \int_0^{2\pi} f^{\mathrm{S}}_{pk}(\phi)\,\mathrm{d}\phi, \quad p, k = 1, 2,3 \tag{27}$$

$$g^{\mathrm{R}}_{pk}(\mathbf{x}, \omega) = \int_0^{2\pi}\int_0^{1} f^{\mathrm{R}}_{pk}(\phi, b, \omega)\,\mathrm{d}\phi\,\mathrm{d}b, \quad p, k = 1, 2, 3 \tag{28}$$

where the integrand functions f^{S}_{pk} and f^{R}_{pk} are known [11]. Similarly, the stress Green's functions are of the form

$$h_{ijk}(\mathbf{x}, \omega) = h^{\mathrm{S}}_{ijk}(\mathbf{x}) + h^{\mathrm{R}}_{ijk}(\mathbf{x}, \omega) \tag{29}$$

Here

$$h^{\mathrm{S}}_{ijk}(\mathbf{x}) = \int_0^{2\pi} f^{\mathrm{S}}_{ijk}(\phi)\,\mathrm{d}\phi, \quad i, j, k = 1, 2, 3 \tag{30}$$

$$h^{\mathrm{R}}_{ijk}(\mathbf{x}, \omega) = \int_0^{2\pi}\int_0^{1} f^{\mathrm{R}}_{ijk}(\phi, b, \omega)\,\mathrm{d}\phi\,\mathrm{d}b, \quad i, j, k = 1, 2, 3 \tag{31}$$

and the functions f^{S}_{ijk} and f^{R}_{ijk} are known [11].

By evaluating simultaneously the entire elastodynamic state vectors for the Green's function displacements or stresses, Dravinski and Zheng [17] proposed an efficient algorithm for evaluation of the elements of the system of equations (21). This procedure avoids repeated calculations of the functions needed to perform the numerical integrations. For details of the proposed method the reader is referred to Reference [17]. Based on that technique the elements of Equation (21) can be determined in order to compute the unknown scattered wave field.

4.2. Numerical integration

One- and two-dimensional composite Newton–Cotes quadratures can be defined as [18]

$$\int_a^b f(x)\,\mathrm{d}x \approx Q_x \equiv (b - a)\mathbf{w}^{\mathrm{T}}\mathbf{f}$$

$$\mathbf{w}^{\mathrm{T}} \equiv [w_1, \ldots, w_{N_x}]; \mathbf{f}^{\mathrm{T}} \equiv [f(x_1), \ldots, f(x_{N_x})] \tag{32}$$

$$\int_a^b \mathrm{d}x \int_c^d f(x, y)\,\mathrm{d}y \approx Q_{xy} \equiv (b-a)(d-c)\mathbf{w}^{\mathrm{T}}\mathbf{F}\boldsymbol{\mu}$$

$$\mathbf{F} \equiv [f(x_i, y_j)], \quad 1 \leqslant i \leqslant N_x, \quad 1 \leqslant j \leqslant N_y \tag{33}$$

$$\boldsymbol{\mu}^{\mathrm{T}} = [\boldsymbol{\mu}_1, \ldots, \mu_{N_y}]$$

where the superscript T denotes the transpose and

$$\begin{aligned} N_x &= n_x(m_x - 1) + 1 \\ N_y &= n_y(m_y - 1) + 1 \end{aligned} \tag{34}$$

Here, n_x and m_x denotes the number of panels and number of points in each panel in the x-direction with corresponding values n_y and m_y in the y-direction. Thus N_x represents the total number of nodes in the x-direction where the integrand is to be evaluated and similarly for N_y. It should be noted that for the quadrature rules given by Equations (32) and (33), the integrand function is computed at each node only once [18]. Similar quadrature rules can be developed using integration formulas of Gauss–Legandre type as well.

4.3. Auxiliary surfaces

The auxiliary surfaces $C^{(J)}$; $J = 1, 2$ which arise in the indirect boundary integral formulation of the problem are defined as the surfaces over which the sources are distributed in such a way to generate the unknown scattered wave field [14]. In general, the auxiliary surfaces $C^{(1)}$ and $C^{(2)}$ are defined inside and outside of the scatterer, respectively. They usually follow in shape the boundary of the scatterer and the distance from the scatterer and the auxiliary surfaces must be

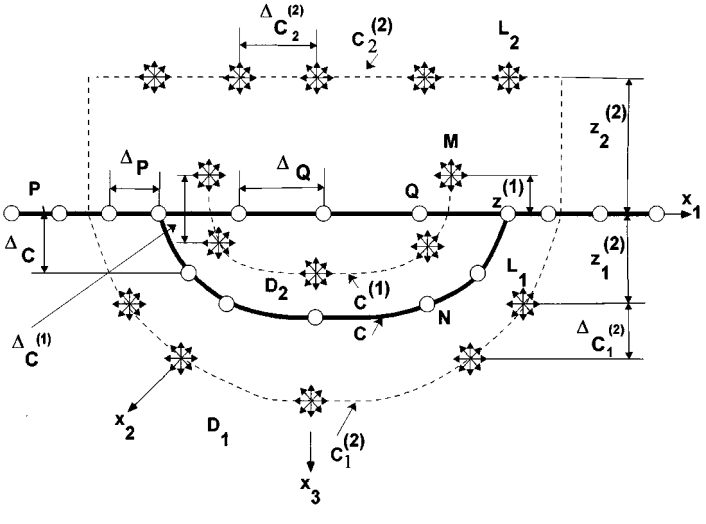

Figure 2. Collocation points and auxiliary surfaces.

determined empirically [16, 19] in order to produce the convergent results for smallest number of sources and collocation points. In this paper the auxiliary surfaces have been constructed by first scaling the interface C, and then by shifting the new surface in the vertical direction. Therefore, the auxiliary surface $C^{(1)}$ is obtained by scaling the interface C with a factor $0 < \xi < 1$ and by shifting the resulting surface for an amount $z^{(1)}$ in the negative $x_3 -$ direction (see Figure 2). Similarly, the auxiliary surface $C^{(2)}$ is obtained by first scaling the interface C with a factor $\eta > 1$ and then by shifting the resulting surface for an amount $z_1^{(2)}$ in the positive $x_3 -$ direction. The resulting surface is then closed in the region $x_3 < 0$ as shown by Figure 2. Thus, the auxiliary surface $C^{(2)}$ consists essentially of two distinct parts: $C_1^{(2)}$ that follows in shape the interface C, and $C_2^{(2)}$ which is parallel to the surface of the half-space.

Let x_C denote the points on the interface C between the basin and the half-space, i.e.

$$x_C \in C \tag{35}$$

Then the auxiliary surfaces can be defined as

$$C^{(1)}: \mathbf{x}_{C^{(1)}} = \xi \mathbf{x}_C + (0, 0, -z^{(1)})^{\mathrm{T}} \tag{36}$$

$$C^{(2)}: \mathbf{x}_{C^{(2)}} = \begin{cases} C_1^{(2)}: \eta \mathbf{x}_C + (0, 0, z_1^{(2)}), & x_3 > 0 \\ C_2^{(2)}: x_3 = -z_2^{(2)}, & \text{otherwise} \end{cases} \tag{37}$$

$$0 < \xi < 1; \quad z^{(1)} > 0; \quad 1 < \eta; \quad z_1^{(2)} > 0, \quad z_2^{(2)} > 0$$

where parameters ξ, η, $z^{(1)}$, $z_1^{(2)}$, and $z_2^{(2)}$ are to be specified.

4.4. Location of collocation and source points

Collocation points along the interface C are used to impose the continuity of displacement and traction fields. Since the Green's functions used to represent the scattered waves are full-space fundamental solutions, the stress free boundary conditions must be enforced at the collocation points along the half-space surface as well.

The point sources, on the other hand, are located along the auxiliary surfaces $C^{(1)}$ and $C^{(2)}$.

4.4.1. Collocation points

Interface of the basin: The collocation points on the basin interface C are placed on curves obtained by intersecting C with the planes $x_3 =$ const. at equally spaced depths of the valley, i.e.

$$\begin{aligned} x_n^{(i)} &= \mathbf{x}_C(x_1, x_2, (i-1)\Delta_C), \quad i = 1, \ldots, N_C, \quad n = 1, \ldots, N_C^{(i)} \\ \Delta_C &= \frac{H_{\max}}{N_C - 1}; \quad N_C^{(1)} + \cdots + N_C^{(N_C)} = N \end{aligned} \tag{38}$$

where N_C, $N_C^{(i)}$, N and $H_{\max}$ denote the number of curves, number of points per each curve, total number points, and the maximum depth of the interface C, respectively. Therefore, the first collocation curve is located at $z_3 = 0$, containing $N^{(1)}$ number of points, while the last curve is located at $z_3 = H_{\max}$ and it contains only one point. The total number of collocation points adds up to N.

Half-space surface: The collocation points along the half-space surface are used to enforce the stress free boundary conditions for the scattered waves. Two regions are distinguished: The bedrock region, $\mathbf{x} \in D_1$, and the basin, $\mathbf{x} \in D_2$. In both regions the collocation curves follow in

shape the surface edge contour of the basin. Therefore, in the bedrock region the collocation curves are defined by

$$\begin{aligned} &\mathbf{x}_p^{(i)} = (1 + (i-1)\Delta_P)\mathbf{x}_C(x_1, x_2, 0), \quad i = 1, \ldots, N_P, \quad p = 1, \ldots, P^{(i)} \\ &P = P^{(1)} + \cdots + P^{(N_P)}, \quad \mathbf{x}_p^{(i)} \in \mathbf{D}_1 \end{aligned} \tag{39}$$

where N_P and $P^{(i)}$ denote the total number of curves and the number of points per each curve, respectively while Δ_P represents spacing between the curves. It should be noted that in order to ensure sufficient accuracy, the stress free boundary conditions in domain D_1 should be enforced over the region spanning at least one width of the valley on each side of the basin.

Similarly, for the basin region, $x_3 = 0$, the collocation curves are defined by

$$\begin{aligned} &\mathbf{x}_q^{(i)} = (1 + (i-1)\Delta_Q)\mathbf{x}_C(x_1, x_2, 0), \quad i = 1, \ldots, N_Q, \quad q = 1, \ldots, Q^{(i)} \\ &Q = Q^{(1)} + \cdots + Q^{(N_Q)}, \quad \mathbf{x}_q^{(i)} \in \mathbf{D}_2 \end{aligned} \tag{40}$$

where N_Q and $Q^{(i)}$ denote the total number of curves and the number of collocation points, respectively, while Δ_Q denotes the spacing between the collocation curves. Therefore, the first collocation curve $\mathbf{x}_q^{(1)} = \mathbf{x}_C(x_1, x_2, 0)$ is the surface edge curve of the basin while the last curve $\mathbf{x}_q^{(1)}$ degenerates to a single point.

This concludes the discussion about the collocation points. The distribution of sources along the auxiliary surfaces is considered next.

4.4.2. Sources

Auxiliary surface $C^{(1)}$: The sources along this auxiliary surface are placed along the curves obtained by intersecting $C^{(1)}$ with planes $x_3 = \text{const.}$ equally spaced with the depth, i.e.

$$\begin{aligned} &x_m^{(i)} = \mathbf{x}_{C^{(1)}}(x_1, x_2, -z^{(1)} + (i-1)\Delta_{C^{(1)}}), \quad i = 1, \ldots, N_{C^{(1)}}, \quad m = 1, \ldots, M^{(i)} \\ &M = M^{(1)} + \cdots + M^{(N_{C^{(1)}})} \end{aligned} \tag{41}$$

where $\Delta_{C^{(1)}}$ denotes the vertical spacing while $N_{C^{(1)}}$ and $M^{(i)}$ represent the number of curves and the number of sources per curve, respectively. The total number of sources along $C^{(1)}$ adds up to M.

Auxiliary surface $C^{(2)}$: For this auxiliary surface one distinguishes two regions: region $C_1^{(2)}$denotes the portion of the surface $C^{(2)}$ for which $x_3 \geqslant z_1^{(2)}$, and region $C_2^{(2)}$ describing the part of surface $C^{(2)}$ for which $x_3 = -z_2^{(2)}$. In region $C_1^{(2)}$ the sources are uniformly distributed along $N_{C_1^{(2)}}$ curves defined by

$$\begin{aligned} &x_{l_1}^{(i)} = \mathbf{x}_{C_1^{(2)}}(x_1, x_2, z_2^{(2)} + (i-1)\Delta_{C_1^{(2)}}), \quad i = 1, \ldots, N_{C_1^{(2)}}, \quad \ell_1 = 1, \ldots, L_1^{(i)} \\ &L_1 = L_1^{(1)} + \cdots + L_1^{(N_{C_1^{(2)}})} \end{aligned} \tag{42}$$

where $\Delta_{C_1^{(2)}}$ denotes the spacing of the curves with the depth while $N_{C_1^{(2)}}$ and $L_1^{(i)}$ denote the number of curves and the number of sources per curve, respectively. The total number of sources for region $C_1^{(2)}$ is denoted by L_1.

For region $C_2^{(2)}$ the sources are distributed along $N_{C_2^{(2)}}$ curves according to

$$\begin{aligned} &x_{l_2}^{(i)} = (1 - i\Delta_{C_2^{(2)}})\mathbf{x}_{C^{(2)}}(x_1, x_2, -z_1^{(2)}), \quad i = 1, \ldots, N_{C_2^{(2)}}, \quad \ell_2 = 1, \ldots, L_2^{(i)} \\ &L_2 = L_2^{(1)} + \cdots + L_2^{(N_{C_2^{(2)}})} \end{aligned} \tag{43}$$

where $\Delta_{C_2^{(2)}}$ denotes the spacing between the curves. The total number of sources for the second region is denoted by L_2 while $L_2^{(i)}$ and $N_{C_2^{(2)}}$ represent the number of sources per each curve and the total number of curves, respectively. It was found that an efficient placement of the sources for region $C_2^{(2)}$ is in the part of $C_2^{(2)}$ which is directly above the basin.

4.5. Convergence criteria

Several numerical parameters present in the problem must be determined in order to calculate the expansion coefficients for the unknown scattered wave field. These include:

(1) Number of collocation points N along the interface C where the continuity of displacement and traction fields is imposed,
(2) number of sources M and L along the auxiliary surfaces $C^{(1)}$ and $C^{(2)}$, respectively,
(3) number of collocation points P and Q along the surface $x_3 = 0$ for domains $D^{(1)}$ and $D^{(2)}$, respectively where the stress free boundary conditions are imposed, and
(4) parameters ξ, η, $z^{(1)}$, $z_1^{(2)}$ and $z_2^{(2)}$ which define the auxiliary surfaces $C^{(1)}$ and $C^{(2)}$.

From the past experience in modeling wave scattering in isotropic media [2] the skewness of matrix $\mathbf{A}$ in Equation (21) is chosen to be $3(P + Q + 2N) : 3(M + L) = 2.5$. Since at present time for anisotropic models studied in this paper no solutions are available, the numerical parameters which produce convergent results are determined by performing the following tests:

1. Isotropic transparency test involves calculation of surface response when the half space and the basin are assumed to be isotropic with the same properties. The parameters are adjusted in such a way to produce the free field response in an isotropic half-space. This provides the initial choice of the parameters needed for evaluation of the scattered wave field.
2. Isotropic limit case test involves evaluation of surface response when the half-space and the basin are assumed to be made of different isotropic materials. For a given incident wave the preliminary numerical parameters determined in Test 1 are adjusted to match the surface response of the corresponding isotropic model.
3. Anisotropic transparency test consists of evaluating surface response when the materials of the half-space and the basin are assumed to be anisotropic and the same. The parameters are chosen to produce the free field response for an anisotropic half-space.
4. Final test consists of calculating surface response when the half-space and the basin are made of different anisotropic materials. The parameters are adjusted in such a way to minimize the norm given by

$$\|\mathbf{Ag} - \mathbf{w}\|^2 \tag{44}$$

where the matrices in the above equation are defined by Equation (21).

It should be pointed out that the first two tests were performed only because the isotropic results were readily available. However, once the basic understanding of how various parameters affect the convergence is achieved, the first two convergence tests may be omitted.

4.6. Isotropic limit test case: a semispherical basin

As an illustration of the isotropic limit test, and the values of numerical parameters present in the problem, the case of a semispherical basin of unit radius subjected to a vertical incident plane

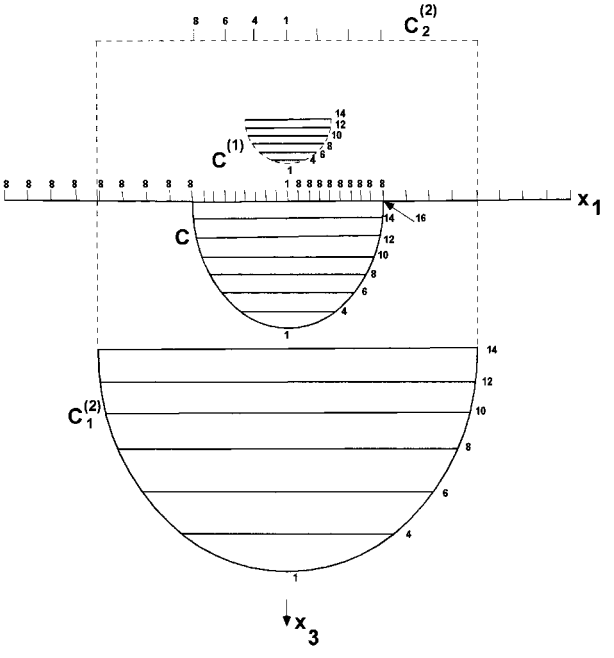

Figure 3. Collocation and source curves used for response calculation of a semispherical basin of unit radius. The numbers denote the collocation points and sources per each circle. Collocation points along C: N = 71, $N_C = 8$, $\Delta_C = \frac{1}{7}$. Collocation points along $x_3 = 0$: $P = 72$, $N_P = 9$, $P^{(i)} = 8$, $i = 1, \ldots, 9$, $\Delta_P = \frac{2}{8}$; $Q = 73$, $N_Q = 9$, $\Delta_Q = \frac{1}{8}$. Auxiliary surfaces and sources: $\xi = 0.2$, $\eta = 1.8$, $z^{(1)} = 0.4$, $z_1^{(2)} = 0.9$, $z_2^{(2)} = 1.5$, $M = 55$, $N_{C^{(1)}} = 7$, $\Delta_{C^{(1)}} = \xi/7$, $L = L_1 + L_2 = 55 + 19 = 74$, $N_{C_1^{(2)}} = 8$, $\Delta_{C_2^{(2)}} = \eta/7$. $N_{C_2^{(2)}} = 4$, $\Delta_{C_2^{(2)}} = \frac{1}{3}$. Quadrature parameters: $m = 9$, $n_b = n_\phi = 20$.

harmonic P-wave is considered next. This problem was originally solved by Sanches-Sesma [20] and subsequently tested by several researchers (e.g. [2]). First, the paramaters used for the numerical evaluation of the results are specified.

The collocation and the source curves for this problem are depicted by Figure 3. Along the interface C, the collocation points are placed along eight circles, $N_C = 8$, with the vertical spacing $\Delta_C = 1/7$. The number of collocation points, equally distributed along each curve, are given by

$$N_C^{(i)} = \begin{cases} 16 - 2(i-1), & i = 1, \ldots, 7 \\ 1, & i = 8 \end{cases}$$

These numbers are shown in Figure 3 along the interface C making the total of $N = 71$ collocation points.

The collocation points on the half-space surface $x_3 = 0$, $1 \leqslant \sqrt{x_1^2 + x_2^2} \leqslant 3$ are placed along nine circles each containing eight points ($N_P = 9$, $P^{(i)} = 8$, i = $1, \ldots, 9$) making total of $P = 72$ points. The separation distance between the circles is $\Delta_P = \frac{2}{8}$. Similarly, the collocation curves

atop the basin consist of nine concentric circles each containing eight points and an additional point is placed at the origin ($N_Q = 10, Q^{(i)} = 8, i = 1, \ldots, 9, Q^{(10)} = 1, \Delta_Q = \frac{1}{9}$) making total of $Q = 73$ points.

The sources along the auxiliary surface $C^{(1)}$ are placed along seven circles, $N_{C^{(1)}} = 7$, with the number of sources distributed along each circle according to (Figure 3)

$$M^{(i)} = \begin{cases} 14 - 2(i-1), & i = 1, \ldots, 6 \\ 1, & i = 7 \end{cases}$$

making total of $M = 55$ sources. Vertical separation for the circles is $\Delta_{C^{(1)}} = \xi/6$.

For the portion of the auxiliary surface $C_1^{(2)}$, the sources are placed along seven circles, $N_{C_1^{(2)}} = 7$, separated vertically by $\Delta_{C_1^{(2)}} = \eta/6$. Per each curve the sources are distributed according to

$$L_1^{(i)} = \begin{cases} 14 - 2(i-1), & i = 1, \ldots, 6 \\ 1, & i = 7 \end{cases}$$

making total of $L_1 = 55$ sources.

Finally, the sources along the portion of the auxiliary surface $C_2^{(2)}$, are located along four circles, $N_{C_1^{(2)}} = 4$, separated by $\Delta_{C_2^{(2)}} = \frac{1}{3}$ with the number of sources per each circle given by

$$L_2^{(i)} = \begin{cases} 8 - 2(i-1), & i = 1, \ldots, 3 \\ 1, & i = 4 \end{cases}$$

making total of $L_2 = 19$ sources.

This completes the description of the parameters used in the numerical evaluation of the results. Based on these parameters, the response of a semispeherical basin of unit radius and subjected to a vertically incident plane harmonic P-wave is evaluated as a limit case when the materials become isotropic. The results of the test, depicted by Figure 4, show very good agreement between the two calculations. Similar tests have been performed for semispeherical and semiprolate basins subjected to different incident waves. These problems, originally solved by Mossessian and Dravinski [2] and Eshraghi and Dravinski [3], provided the limit test cases for a large class of problems. The results of these tests as well as the transparency and final tests are omitted for the sake of reducing the number of figures. Consequently, the response of an anisotropic basin is considered next.

5. RESPONSE OF AN ANISOTROPIC BASIN

In order to study the role of anisotropy on the basin's response it is necessary first to choose the material properties for the half-space and the basin. The model consists of a beryl half-space and a beryl-like basin with the material properties given by Table I (all normalized with respect C_{44} of the half-space).

The surface response for a semispherical basin of unit radius subjected to different incident pseudo-P-waves is depicted by Figure 5. The first and second columns denote the surface response along the lines $(x, 0, 0)$ and $(0, y, 0)$, respectively.

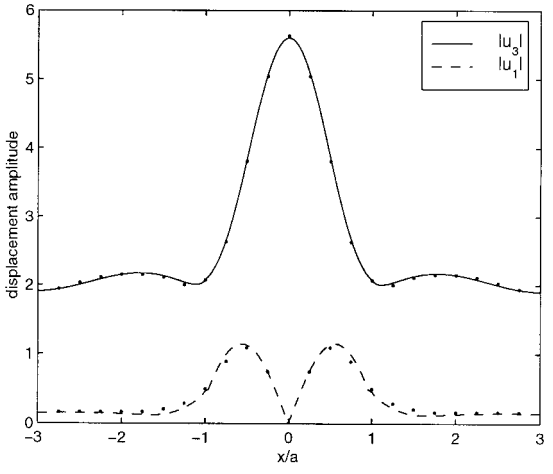

Figure 4. Convergence test. Surface response spectral amplitude of a semispherical isotropic basin of unit radius ($a = 1$) subjected to a vertical plane harmonic P-wave. Response is evaluated along the axis $(x_1, x_2, x_3) = (x, 0, 0)$. Solid and dash lines denotes the results of this study while dots represent the results of Reference 14. P-wave velocities: $\alpha_1 = 1.732$, $\alpha_2 = 1.414$; shear moduli: $\mu_1 = 1$, $\mu_2 = 0.3$; circular frequency: $\omega = 2.72\,\mathrm{s}^{-1}$. Collocation points, auxiliary surfaces, and sources are the same as in Figure 3.

Table I. Material properties for Model 1.

Model	ρ	C_{11}	C_{12}	C_{13}	C_{33}	C_{44}
Half-space	1	4.13	1.47	1.01	3.62	1
Basin	0.67	1.38	0.49	0.337	1.26	0.33

For different incident pseudo SV- SH-, and Rayleigh waves the surface response of a semispherical basin is shown by Figures 6 and 8, respectively. The amplitude of the incident waves are chosen in such a way that as the materials become isotropic the free field reduces to the corresponding isotropic free field as given by Reference 21. It is apparent from these results that the presence of the basin significantly changes the surface response. In addition, the response is very sensitive upon the nature of the incident wave (type, angle, and frequency), and the location of the observation station. Significant mode conversion may be detected which is not present in 2D models.

Similar results were obtained for a semiprolate basin and they are omitted for the sake of reducing the number of figures.

In order to assess the importance of anisotropy on surface ground motion amplification the isotropic semispherical basin of unit radius are reexamined for incident plane harmonic

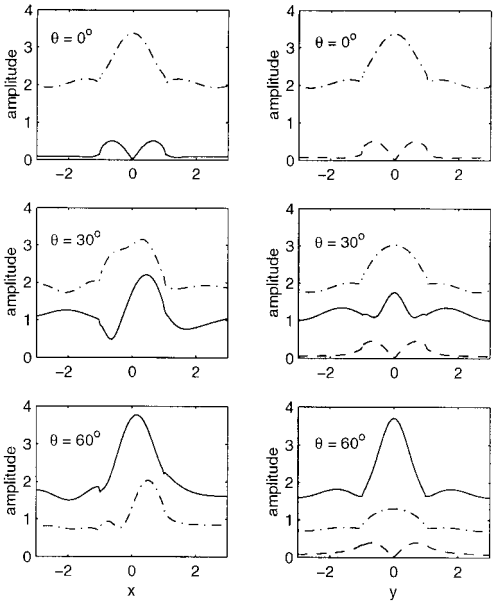

Figure 5. Surface response spectral amplitude of a unit semispherical transversely isotropic basin subjected to different incident plane harmonic pseudo-P-waves along the two axis $(x_1, x_2, x_3) = (x, 0, 0)$ and $(x_1, x_2, x_3) = (0, y, 0)$. The angles of incidence: $\theta^{\text{inc}} = 0^\circ$, 30°, 60°; $\phi^{\text{inc}} = 0$. $\omega = 0.951\pi(s^{-1})$. Collocation points, auxiliary surfaces, and sources are the same as in Figure 3. u_1 (solid lines), u_2 (dash lines), u_3 (dash–dot lines). Amplitude of the incident wave: $U_{12} = 1$ for $\theta^{\text{inc}} = 0^\circ$, $U_{12} = -\sin\theta^{\text{inc}}$ for $\theta^{\text{inc}} \neq 0$.

P-, SV-, SH-, and Rayleigh waves. The material properties for the isotropic model are chosen as

$$\lambda^{(1)} + 2\mu^{(1)} = \frac{C_{11}^{(1)} + C_{22}^{(1)} + C_{33}^{(1)}}{3} = 3.96$$

$$\mu^{(1)} = C_{44}^{(1)} = C_{55}^{(1)} = C_{66}^{(1)} = \rho^{(1)} = 1$$

$$C_{12}^{(1)} = C_{13}^{(1)} = C_{23}^{(1)} = \lambda^{(1)} = 1.96$$

$$\lambda^{(2)} + 2\mu^{(2)} = \frac{C_{11}^{(2)} + C_{22}^{(2)} + C_{33}^{(2)}}{3} = 1.32$$

$$\mu^{(2)} = C_{44}^{(2)} = C_{55}^{(2)} = C_{66}^{(2)} = 0.333, \quad \rho^{(2)} = 0.667$$

$$C_{12}^{(2)} = C_{13}^{(2)} = C_{23}^{(2)} = \lambda^{(2)} = 0.653$$

where λ and μ denote the Lamé constants. For incident P- and SV-waves the results for isotropic basin are depicted by Figures 9 and 10. Comparison of anisotropic responses (Figures 5 and 6) with the isotropic ones (Figures 9 and 10) shows that the peak amplitudes of surface motion are similar while the details of the displacement patterns may be quite different for the two models.

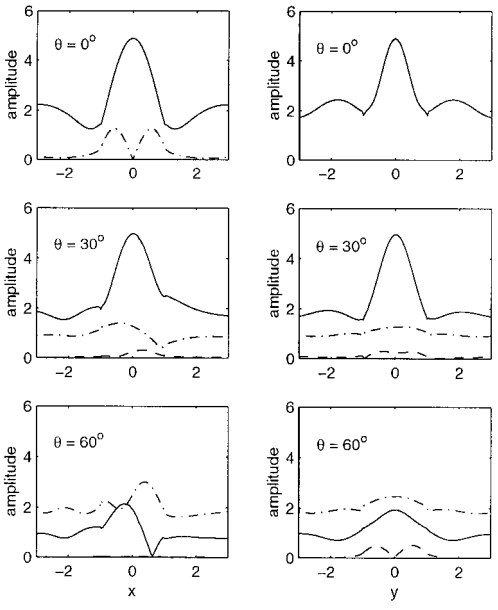

Figure 6. Surface response spectral amplitude of a unit semispherical transversely isotropic basin subjected to different incident plane harmonic pseudo-SV-waves along the two axis $(x_1, x_2, x_3) = (x, 0, 0)$ and $(x_1, x_2, x_3) = (0, y, 0)$. The angles of incidence: $\theta^{\text{inc}} = 0^\circ$, 30°, 60°; $\phi^{\text{inc}} = 0^\circ$. $\omega = 0.951\pi(s^{-1})$. Collocation points, auxiliary surfaces, and sources are the same as in Figure 3. u_1 (solid lines), u_2 (dash lines), u_3 (dash–dot lines). Amplitude of the incident wave: $U_{14} = 1$ for $\theta^{\text{inc}} = 0^\circ$, $U_{14} = \cos\theta^{\text{inc}}$ for $\theta^{\text{inc}} \neq 0$.

These differences may be particularly significant for oblique incidences. Similar conclusions have been reached for incident SH- and Rayleigh waves and these results were omitted in order to reduce the number of figures. Therefore, presented results clearly demonstrate that the anisotropy may play significant role in amplification of surface ground motion of the basin.

6. SUMMARY AND CONCLUSIONS

Scattering of elastic waves by a three-dimensional basin embedded within an elastic half-space has been considered by using an indirect boundary integral equation approach. The materials were assumed to be transversely isotropic, while the incident waves were plane harmonic pseudo P-, SV-, SH-, and Rayleigh waves. The unknown scattered waves were described in terms of full-space Green's functions for anisotropic media. The scattered waves were determined by satisfying the stress free boundary conditions (along the half-space surface) and the continuity conditions (between the basin and the half-space) in a least-squares sense.

Convergence of the method has been discussed in detail and the surface response spectral amplitudes have been presented for a semispherical basin and various incident waves. The results

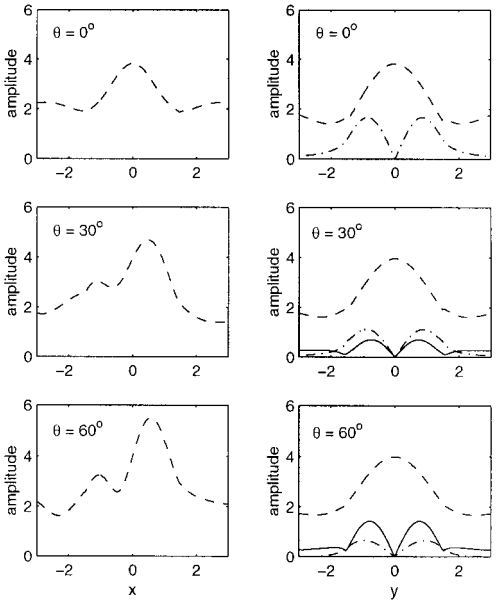

Figure 7. Surface response spectral amplitude of a unit semispherical transversely isotropic basin subjected to oblique incident plane harmonic pseudo-SH-waves along the two axis $(x_1, x_2, x_3) = (x, 0, 0)$ and $(x_1, x_2, x_3) = (0, y, 0)$. The angles of incidence: $\theta^{\text{inc}} = 0^\circ$, 30°, 60°; $\phi^{\text{inc}} = 0^\circ$. $\omega = 0.951\pi(s^{-1})$. Collocation points, auxiliary surfaces, and sources are the same as in Figure 3. u_1 (solid lines), u_2 (dash lines), u_3 (dash–dot lines). Amplitude of the incident wave: $U_{26} = 1$.

clearly demonstrate that the presence of the basin may cause significant amplification of surface ground motion. The level of amplification depends upon the nature of incident wave, shape and material properties of the basin, and the location of the observation point.

Although the response comparison between anisotropic and isotropic models shows similar peak amplitudes, the differences in surface motion pattern between the two models may be considerable especially for a non-vertical incidence. This clearly demonstrates the importance of material anisotropy in amplification of surface ground motion.

APPENDIX

Matrices $\mathbf{H}^{(1)}$ and $\mathbf{H}^{(2)}$ are defined by

$$\mathbf{H}^{(1)} = \begin{bmatrix} [h^{(1)}_{311}(\mathbf{x}_p, \mathbf{x}_m)] \\ [h^{(1)}_{231}(\mathbf{x}_p, \mathbf{x}_m)] \\ [h^{(1)}_{331}(\mathbf{x}_p, \mathbf{x}_m)] \end{bmatrix} \begin{bmatrix} [h^{(1)}_{312}(\mathbf{x}_p, \mathbf{x}_m)] \\ [h^{(1)}_{232}(\mathbf{x}_p, \mathbf{x}_m)] \\ [h^{(1)}_{332}(\mathbf{x}_p, \mathbf{x}_m)] \end{bmatrix} \begin{bmatrix} [h^{(1)}_{313}(\mathbf{x}_p, \mathbf{x}_m)] \\ [h^{(1)}_{233}(\mathbf{x}_p, \mathbf{x}_m)] \\ [h^{(1)}_{333}(\mathbf{x}_p, \mathbf{x}_m)] \end{bmatrix} \tag{A1}$$

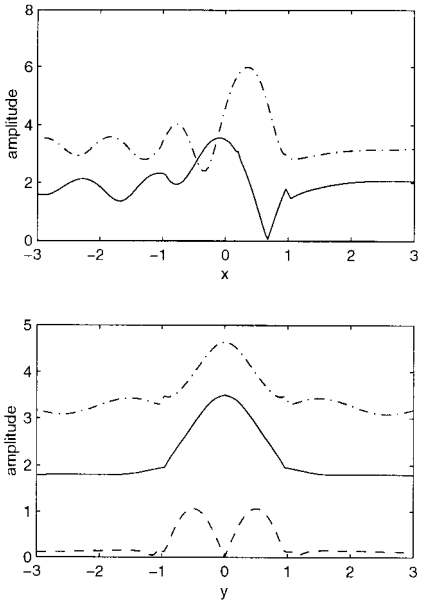

Figure 8. Surface response spectral amplitude of a unit semispherical transversely isotropic basin subjected to incident plane harmonic pseudo-Rayleigh-waves along the two axis $(x_1, x_2, x_3) = (x, 0, 0)$ and $(x_1, x_2, x_3) = (0, y, 0)$. $\omega = 951\pi(s^{-1})$. Collocation points, auxiliary surfaces, and sources are the same as in Figure 3. u_1 (solid lines), u_2 (dash lines), u_3 (dash–dot lines). Amplitude of the incident wave: $U_{11} = 2.3$.

$$\mathbf{H}^{(2)} = \begin{bmatrix} [h^{(2)}_{311}(\mathbf{x}_q, \mathbf{x}_\ell)] \\ [h^{(2)}_{231}(\mathbf{x}_q, \mathbf{x}_\ell)] \\ [h^{(1)}_{331}(\mathbf{x}_q, \mathbf{x}_\ell)] \end{bmatrix} \begin{bmatrix} [h^{(2)}_{312}(\mathbf{x}_q, \mathbf{x}_\ell)] \\ [h^{(2)}_{232}(\mathbf{x}_q, \mathbf{x}_\ell)] \\ [h^{(2)}_{332}(\mathbf{x}_q, \mathbf{x}_\ell)] \end{bmatrix} \begin{bmatrix} [h^{(2)}_{313}(\mathbf{x}_q, \mathbf{x}_\ell)] \\ [h^{(2)}_{233}(\mathbf{x}_q, \mathbf{x}_\ell)] \\ [h^{(2)}_{333}(\mathbf{x}_q, \mathbf{x}_\ell)] \end{bmatrix} \tag{A2}$$

where $\mathbf{x}_p \in \{D_1 | x_3 = 0; p = 1, \ldots, P\}$, $\mathbf{x}_q \in \{D_2 | x_3 = 0; q = 1, \ldots, Q\}$, $\mathbf{x}_m \in C^{(1)}$; $m = 1, \ldots, M$ and $\mathbf{x}_\ell \in C^{(2)}$; $\ell = 1, \ldots, L$. The submatrices $[h^{(1)}_{ijk}(\mathbf{x}_p, \mathbf{x}_m)]$ are simply obtained by evaluating stress Green's functions $h^{(1)}_{ijk}$ at $(\mathbf{x}_p, \mathbf{x}_m)$ while $[h^{(2)}_{ijk}(\mathbf{x}_p, \mathbf{x}_\ell)]$ denote submatrices obtained through evaluation of the Green's function $h^{(2)}_{ijk}$ at $(\mathbf{x}_p, \mathbf{x}_\ell)$.

The matrices $\mathbf{G}^{(1)}$, $\mathbf{G}^{(2)}$, and vector $\mathbf{u}^{(1)\mathrm{ff}}$ are defined by

$$\mathbf{G}^{(1)} = \begin{bmatrix} [G^{(1)}_{11}(\mathbf{x}_n, \mathbf{x}_m)] & [G^{(1)}_{12}(\mathbf{x}_n, \mathbf{x}_m)] & [G^{(1)}_{13}(\mathbf{x}_n, \mathbf{x}_m)] \\ [G^{(1)}_{21}(\mathbf{x}_n, \mathbf{x}_m)] & [G^{(1)}_{22}(\mathbf{x}_n, \mathbf{x}_m)] & [G^{(1)}_{23}(\mathbf{x}_n, \mathbf{x}_m)] \\ [G^{(1)}_{31}(\mathbf{x}_n, \mathbf{x}_m)] & [G^{(1)}_{32}(\mathbf{x}_n, \mathbf{x}_m)] & [G^{(1)}_{33}(\mathbf{x}_n, \mathbf{x}_m)] \end{bmatrix}$$

$$\mathbf{G}^{(2)} = \begin{bmatrix} [G^{(2)}_{11}(\mathbf{x}_n, \mathbf{x}_\ell)] & [G^{(2)}_{12}(\mathbf{x}_n, \mathbf{x}_\ell)] & [G^{(2)}_{13}(\mathbf{x}_n, \mathbf{x}_\ell)] \\ [G^{(2)}_{21}(\mathbf{x}_n, \mathbf{x}_\ell)] & [G^{(2)}_{22}(\mathbf{x}_n, \mathbf{x}_\ell)] & [G^{(2)}_{23}(\mathbf{x}_n, \mathbf{x}_\ell)] \\ [G^{(2)}_{31}(\mathbf{x}_n, \mathbf{x}_\ell)] & [G^{(2)}_{32}(\mathbf{x}_n, \mathbf{x}_\ell)] & [G^{(2)}_{33}(\mathbf{x}_n, \mathbf{x}_\ell)] \end{bmatrix} \tag{A3}$$

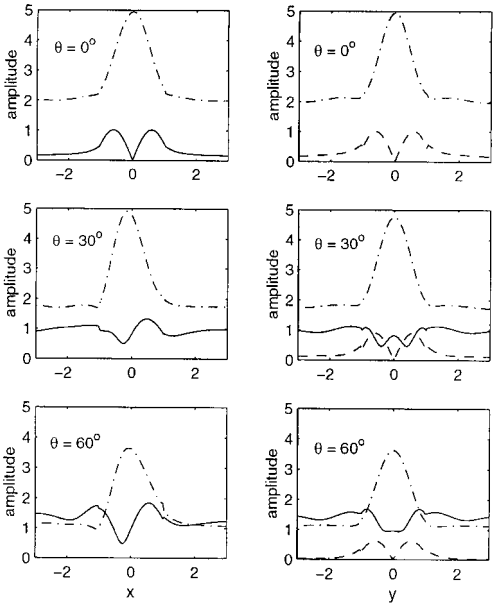

Figure 9. Surface response of a semispherical isotropic basin of unit radius for different incident plane P-harmonic waves along two axes $(x_1, x_2, x_3) = (x, 0, 0)$ and $(x_1, x_2, x_3) = (0, y, 0)$. $\phi^{\text{inc}} = 0^\circ$, $\theta^{\text{inc}} = 0^\circ$, 30°, 60°, $\omega = 0.995\pi(s^{-1})$. $z_1^{(2)} = 1.5$ and collocation points, auxiliary surfaces, and sources are the same as in Figure 3. u_1 (solid lines), u_2 (dash lines), u_3 (dash–dot lines). Amplitude of the incident wave: $U_{12} = 1$ for $\theta^{\text{inc}} = 0^\circ$, $U_{12} = -\sin\theta^{\text{inc}}$ for $\theta^{\text{inc}} \neq 0^\circ$. Material properties defined in the text.

$$\mathbf{u}^{(1))\text{ff}} = \begin{bmatrix} [u_1^{\text{ff}}(\mathbf{x}_n)] \\ [u_2^{\text{ff}}(\mathbf{x}_n)] \\ [u_3^{\text{ff}}(\mathbf{x}_n)] \end{bmatrix} \tag{A4}$$

Here $\mathbf{x}_n \in C$; $n = 1, \ldots, N$; $\mathbf{x}_m \in C^{(1)}$; $m = 1, \ldots, M$; and $\mathbf{x}_\ell \in C^{(2)}$; $\ell = 1, \ldots, L$.

The matrices arising from the traction continuity along the interface C are of the form

$$\mathbf{T}^{(1)} = \begin{bmatrix} \mathbf{X}_a^{(1)} & \mathbf{X}_b^{(1)} & \mathbf{X}_c^{(1)} \\ \mathbf{Y}_a^{(1)} & \mathbf{Y}_b^{(1)} & \mathbf{Y}_c^{(1)} \\ \mathbf{Z}_a^{(1)} & \mathbf{Z}_b^{(1)} & \mathbf{Z}_c^{(1)} \end{bmatrix} \tag{A5}$$

$$\mathbf{T}^{(2)} = \begin{bmatrix} \mathbf{X}_d^{(2)} & \mathbf{X}_e^{(2)} & \mathbf{X}_f^{(2)} \\ \mathbf{Y}_d^{(2)} & \mathbf{Y}_e^{(2)} & \mathbf{Y}_f^{(2)} \\ \mathbf{Z}_d^{(2)} & \mathbf{Z}_e^{(2)} & \mathbf{Z}_e^{(2)} \end{bmatrix} \tag{A6}$$

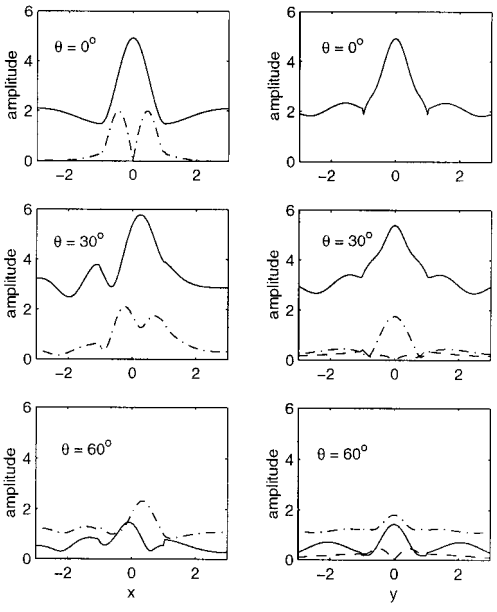

Figure 10. Surface response of a semispherical isotropic basin of unit radius for different incident plane harmonic SV-waves along two axes $(x_1, x_2, x_3) = (x, 0, 0)$ and $(x_1, x_2, x_3) = (0, y, 0)$. $\phi^{\text{inc}} = 0°$, $\theta^{\text{inc}} = 0°$, 30°, 60°, $\omega = 0.995\pi(s^{-1})$. $z_1^{(2)} = 1.5$ and collocation points, auxiliary surfaces, and sources are the same as in Figure 3. u_1 (solid lines), u_2 (dash lines), u_3 (dash–dot lines). Amplitude of the incident wave: $U_{14} = 1$ for $\theta^{\text{inc}} = 0$, $U_{14} = \cos\theta^{\text{inc}}$ for $\theta^{\text{inc}} \neq 0$. Material properties defined in the text.

$$\mathbf{t}^{(1)\text{ff}} = \begin{bmatrix} [t_1^{(1)\text{ff}}(\mathbf{x}_n)] \\ [t_2^{(1)\text{ff}}(\mathbf{x}_n)] \\ [t_3^{(1)\text{ff}}(\mathbf{x}_n)] \end{bmatrix} \tag{A7}$$

The matrices in the above equations are defined by

$$\begin{aligned}
[X_a^{(1)}(\mathbf{x}_n, \mathbf{x}_m)] &= h_{111}^{(1)}(\mathbf{x}_{\underline{n}}, \mathbf{x}_m)\gamma_1(\mathbf{x}_{\underline{n}}) + h_{121}^{(1)}(\mathbf{x}_{\underline{n}}, \mathbf{x}_m)\gamma_2(\mathbf{x}_{\underline{n}}) + h_{131}^{(1)}(\mathbf{x}_{\underline{n}}, \mathbf{x}_m)\gamma_3(\mathbf{x}_{\underline{n}}) \\
[X_b^{(1)}(\mathbf{x}_n, \mathbf{x}_m)] &= h_{112}^{(1)}(\mathbf{x}_{\underline{n}}, \mathbf{x}_m)\gamma_1(\mathbf{x}_{\underline{n}}) + h_{122}^{(1)}(\mathbf{x}_{\underline{n}}, \mathbf{x}_m)\gamma_2(\mathbf{x}_{\underline{n}}) + h_{312}^{(1)}(\mathbf{x}_{\underline{n}}, \mathbf{x}_m)\gamma_3(\mathbf{x}_{\underline{n}}) \\
[X_c^{(1)}(\mathbf{x}_n, \mathbf{x}_m)] &= h_{113}^{(1)}(\mathbf{x}_{\underline{n}}, \mathbf{x}_m)\gamma_1(\mathbf{x}_{\underline{n}}) + h_{123}^{(1)}(\mathbf{x}_{\underline{n}}, \mathbf{x}_m)\gamma_2(\mathbf{x}_{\underline{n}}) + h_{313}^{(1)}(\mathbf{x}_{\underline{n}}, \mathbf{x}_m)\gamma_3(\mathbf{x}_{\underline{n}})
\end{aligned} \tag{A8}$$

$$\begin{aligned}
[Y_a^{(1)}(\mathbf{x}_n, \mathbf{x}_m)] &= h_{211}^{(1)}(\mathbf{x}_{\underline{n}}, \mathbf{x}_m)\gamma_1(\mathbf{x}_{\underline{n}}) + h_{221}^{(1)}(\mathbf{x}_{\underline{n}}, \mathbf{x}_m)\gamma_2(\mathbf{x}_{\underline{n}}) + h_{231}^{(1)}(\mathbf{x}_{\underline{n}}, \mathbf{x}_m)\gamma_3(\mathbf{x}_{\underline{n}}) \\
[Y_b^{(1)}(\mathbf{x}_n, \mathbf{x}_m)] &= h_{212}^{(1)}(\mathbf{x}_{\underline{n}}, \mathbf{x}_m)\gamma_1(\mathbf{x}_{\underline{n}}) + h_{222}^{(1)}(\mathbf{x}_{\underline{n}}, \mathbf{x}_m)\gamma_2(\mathbf{x}_{\underline{n}}) + h_{232}^{(1)}(\mathbf{x}_{\underline{n}}, \mathbf{x}_m)\gamma_3(\mathbf{x}_{\underline{n}}) \\
[Y_c^{(1)}(\mathbf{x}_n, \mathbf{x}_m)] &= h_{213}^{(1)}(\mathbf{x}_{\underline{n}}, \mathbf{x}_m)\gamma_1(\mathbf{x}_{\underline{n}}) + h_{223}^{(1)}(\mathbf{x}_{\underline{n}}, \mathbf{x}_m)\gamma_2(\mathbf{x}_{\underline{n}}) + h_{233}^{(1)}(\mathbf{x}_{\underline{n}}, \mathbf{x}_m)\gamma_3(\mathbf{x}_{\underline{n}})
\end{aligned} \tag{A9}$$

$$
\begin{aligned}
[Z_a^{(1)}(\mathbf{x}_n, \mathbf{x}_m)] &= h_{311}^{(1)}(\mathbf{x}_{\underline{n}}, \mathbf{x}_m)\gamma_1(\mathbf{x}_{\underline{n}}) + h_{321}^{(1)}(\mathbf{x}_{\underline{n}}, \mathbf{x}_m)\gamma_2(\mathbf{x}_{\underline{n}}) + h_{331}^{(1)}(\mathbf{x}_{\underline{n}}, \mathbf{x}_m)\gamma_3(\mathbf{x}_{\underline{n}}) \\
[Z_b^{(1)}(\mathbf{x}_n, \mathbf{x}_m)] &= h_{312}^{(1)}(\mathbf{x}_{\underline{n}}, \mathbf{x}_m)\gamma_1(\mathbf{x}_{\underline{n}}) + h_{322}^{(1)}(\mathbf{x}_{\underline{n}}, \mathbf{x}_m)\gamma_2(\mathbf{x}_{\underline{n}}) + h_{332}^{(1)}(\mathbf{x}_{\underline{n}}, \mathbf{x}_m)\gamma_3(\mathbf{x}_{\underline{n}}) \\
[Z_c^{(1)}(\mathbf{x}_n, \mathbf{x}_m)] &= h_{313}^{(1)}(\mathbf{x}_{\underline{n}}, \mathbf{x}_m)\gamma_1(\mathbf{x}_{\underline{n}}) + h_{323}^{(1)}(\mathbf{x}_{\underline{n}}, \mathbf{x}_m)\gamma_2(\mathbf{x}_{\underline{n}}) + h_{333}^{(1)}(\mathbf{x}_{\underline{n}}, \mathbf{x}_m)\gamma_3(\mathbf{x}_{\underline{n}})
\end{aligned} \tag{A10}
$$

The components of matrix $\mathbf{T}^{(2)}$ can be obtained from the components of matrix $\mathbf{T}^{(1)}$ by replacing in Equations (A8)–(A10) the superscript (1) with (2), and the subscript m with ℓ. As before, $x_n \in C$; $n = 1, \ldots, N$; $\mathbf{x}_m \in C^{(1)}$; $m = 1, \ldots, M$; and $\mathbf{x}_\ell \in C^{(2)}$; $\ell = 1, \ldots, L$.

ACKNOWLEDGEMENTS

The support to T. Zheng from USC All University Predoctoral Merit Fellowship and Department of Mechanical Engineering Teaching Assistantship is greatly appreciated. The authors would like to thank N. N. Biswas of University of Alaska, Fairbanks and Scientific Foundation of Alaska for their support in facilitating part of the computations in this research.

REFERENCES

1. Beskos DE. Boundary element method in dynamic analysis. *Applied Mechanics Reviews*, 1987; **40**(1):1–23.
2. Mossessian TK, Dravinski M. Amplification of elastic waves by a three dimensional valley, Part 2: Transient response. *Earthquake Engineering Structural & Dynamics*, 1990; **19**:681–691.
3. Eshraghi H, Dravinski M. Scattering of elastic waves by three dimensional non-axisymmetric dipping layers. *International Journal for Numerical Methods in Engineering*, 1991; **31**:1009–1026.
4. Bouchon M, Coutant O. Calculation of synthetic seismograms in a laterally varying medium by the boundary element — discrete wavenumber method. *Bulletin of the Seismological Society of America*, 1994; **84**:1869–1881.
5. Stonley R. The seismological implications for aelotropy in continental structure. *Monthly Notices of the Royal Astronomical Society*, *Geophysics Supplement*, 1949; **5**:343–352.
6. Spies M. Green's tensor function for Lamb's problem: the general anisotropic case. *Acoustical Society of America*, *Journal*, 1997; **102**(4):2438–2441.
7. Tewary VK. Inversion of elastic waveform data in anisotropic solids using the delta-function representation of the Green's function. *Acoustical Society of America*, *Journal*, 1998; **104**(3):1716–1719.
8. Achenbach JD, Wang CY, Hirose S. Two-dimensional time domain BEM for scattering of elastic waves in solids of general anisotropy. *International Journal of Solids and Structures*, 1996; **33**:3843–3864.
9. Zheng T, Dravinski M. Amplification of SH waves by an orthotropic basin. *Earthquake Engineering & Structural Dynamics*, 1998; **27**:243–257.
10. Zheng T, Dravinski M. Amplification of waves by an orthotropic basin: Sagittal plane motion. *Earthquake Engineering & Structural Dynamics*, 1999; **28**:565–584.
11. Wang CY, Achenbach JD. Three-dimensional time-harmonic elastodynamic Green's functions for anisotropic solids. *Proceedings of the Royal Society of London A*, 1995; **449**:441–458.
12. Deans SR. *The Radon Transform and Some of Its Applications*. Wiley: New York, 1983.
13. Nayfeh AH. *Wave Propagation in Layered Anisotropic Media*. Elsevier: Amsterdam, 1995.
14. Kupradze VD. *Dynamical Problems in Elasticity*, *Progress in Solid Mechanics*, Vol. 3, North-Holland: Amsterdam, 1963.
15. Ursell F. On the exterior problems of acoustics. *Proceedings of the Cambridge Philosophical Society*, 1973; **74**:117–125.
16. Dravinski M. Scattering of plane harmonic SH waves by dipping layers of arbitrary shape. *Bulletin of the Seismological Society of America*, 1983; **73**:1303–1319.
17. Dravinski M, Zheng T. Numerical evaluation of three-dimensional time-harmonic Green's functions for a non-isotropic full-space. *Wave Motion*, 1999, accepted.
18. Van Loan CF. *Introduction to Scientific Computing*. Prentice-Hall: Englewood Cliffs, NJ, 1997.
19. Mossessian TK, Dravinski M. Amplification of elastic waves by a three dimensional valley, Part 1: steady-state response. *Earthquake Engineering & Structural Dynamics*, 1990; **19**:667–680.
20. Sanchez-Sesma FJ. Diffraction of elastic waves by three dimensional surface irregularities. *Bulletin of the Seismological Society of America*, 1983; **73**:1621–1636.
21. Mal AK. Singh SJ. *Deformation of Elastic Solids*. Prentice-Hall, Englewood Cliffs, NJ, 1991.

